The Aeronautical Journal (2026), 1–18
doi:10.1017/aer.2026.10216

RESEARCH ARTICLE

Experimental investigation of highly aggressive inter-compressor ducts

Stefan Philipp Fritz[1], Alexander Hergt[1], Sebastian Grund[1], Johann Schlappa[1], David Bresemann[2], Mario Eck[2] and Dieter Peitsch[2]

[1]Fan and Compressor, Institute of Propulsion Technology, German Aerospace Center, 51147 Cologne, North Rhine-Westphalia, Germany
[2]Chair of Aero Engines, Institute of Aeronautics and Astronautics, Technical University of Berlin, 10587 Berlin, Germany
Corresponding author: Stefan Philipp Fritz; Email: stefan.fritz@dlr.de

Received: 12 February 2026 UTC; **Revised:** 10 July 2026 UTC; **Accepted:** 21 July 2026 UTC

Keywords: inter-compressor duct (ICD); flow separation; experimental validation; component testing; compressor aerodynamics

Abstract

Testing of enhanced engine components under real engine conditions is still important to validate the design and meet certification requirements. However, testing is expensive and time-consuming. Furthermore, there is a high risk that the numerical design differs from the experimental results. To mitigate this risk, small-scale experiments can be conducted to obtain experimental validation data in an early design stage. The present study evaluates this design strategy on the specific case of a highly aggressive inter-compressor duct (ICD). A highly modular test rig was set up at the Technical University of Berlin (TUB) as a down-scaled twin with a scaling factor of 2.55 of the German Aerospace Center (DLR) ICD rig. Test campaigns of the highly aggressive ICD were conducted on both test rigs. The ICD design is the same, but the adjacent components differ. The design process is traced backward in the present study. Starting from a detailed analysis of the full-scale test campaign, the differences between steady Reynolds-averaged Navier-Stokes (RANS) simulations and the experimental data are evaluated. The losses predicted with the RANS simulation and the Hellsten turbulence model are more than 80% higher than measured. Finally, the results of the down-scaled rig are compared with those of the full-scale rig. Although the extent of the loss regions differs, both rigs show the same loss mechanisms. Therefore, the chosen design approach is effective, particularly when the numerical modeling is subject to high uncertainties.

Nomenclature

ADP	aerodynamic design point
AFC	active flow control
ALF	aft-looking forward
CFD	computational fluid dynamics
HPC	high pressure compressor
ICD	inter compressor duct
IGV	inlet guide vane
LPC	low pressure compressor
MHP	multi-hole probe
OGV	outlet guide vane
PJA	pulsed jet actuator
RANS	Reynolds-averaged Navier-Stokes
RSM	Reynolds-stress model
SST	shear-stress transport

© The Author(s), 2026. Published by Cambridge University Press on behalf of Royal Aeronautical Society. This is an Open Access article, distributed under the terms of the Creative Commons Attribution licence (https://creativecommons.org/licenses/by/4.0/), which permits unrestricted re-use, distribution and reproduction, provided the original article is properly cited.

Downloaded from https://www.cambridge.org/core. 19 Nov 2026 at 16:04:28, subject to the Cambridge Core terms of use.

Greek symbol

α	circumferential flow angle
ω	stagnation pressure loss

1.0 Introduction

In a modern civil jet engine, the core compression system consists of a low-pressure compressor (LPC) and a high-pressure compressor (HPC). The inter-compressor duct (ICD) connects the two compressors. The primary aerodynamic purpose of an ICD is to guide the core mass flow to the lower radius of the HPC. Consequently, the aerodynamic objective of an ICD is to reduce the radius over a short axial length with minimal losses.

However, the objectives are in conflict with each other. By reducing the axial length of an ICD, the curvature of the bends increases. The result is a stronger acceleration around convex surfaces as the hub in the first bend or the shroud in the second bend. The flow on concave surfaces is decelerated. Consequently, the acceleration and deceleration in the bends of an ICD also affect the static pressure field. If the flow is accelerated, the static pressure decreases. The opposite occurs if the flow is decelerated. The result is a pressure field with strong radial and axial pressure gradients, as shown in Fig. 1. With shorter and therefore steeper ICDs, the pressure gradients increase. Especially the strong adverse pressure gradient at the hub is critical and could cause separations on the hub. The effect of length reduction on the flow field of an unstrutted ICD is investigated by Ortiz Dueñas [2]. Furthermore, Naylor [3] concludes that the presence of a strut increases the risk of a corner separation in aggressive ICDs.

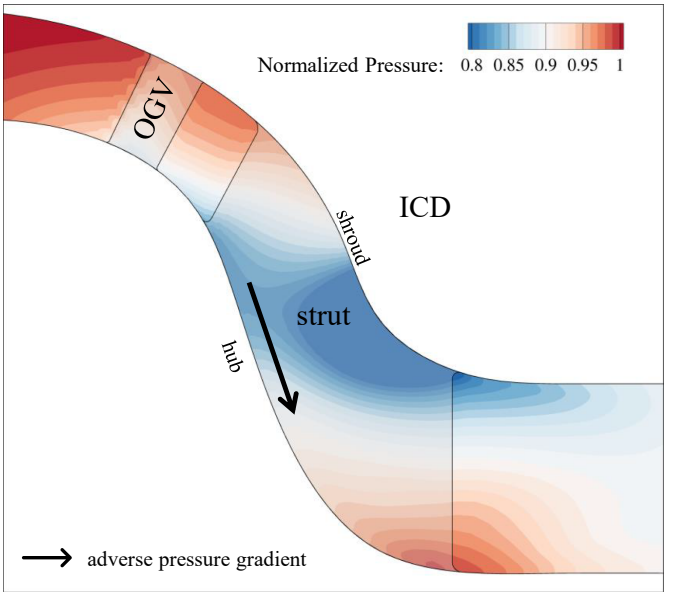
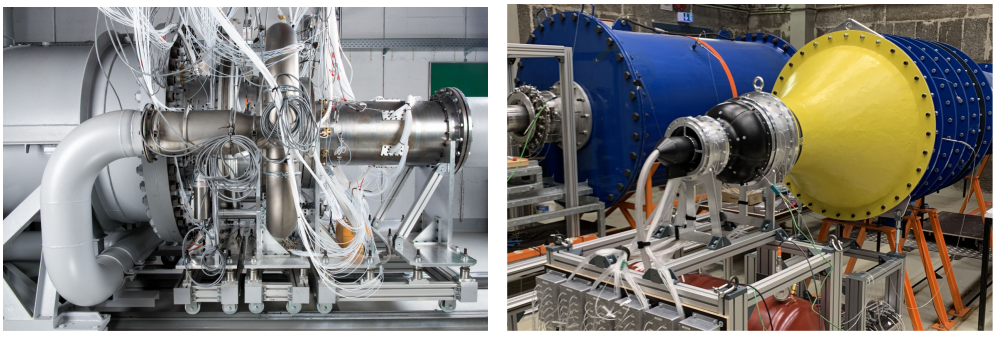


Figure 1. *Circumferentially averaged static pressure field of a highly aggressive ICD on the meridional (S2M) plane (Fritz [1]).*

Other studies focus on synergies between the outlet guide vanes (OGVs) and the struts. Walker [4] reduces the axial length of the ICD by integrating the OGV into the first bend of the duct. Subsequently, Walker [5] tested a turning strut to offload the OGVs and improve the LPC efficiency by a lower reaction. The concept of a turning strut was also explored by Wallin [6]. The turning strut replaces the OGVs and symmetric struts and is designed to remove the remaining swirl from the LPC. Based on Walker's work, Mariah [7] developed a concept in which the ICD can be further shortened by combining the strut with an OGV.

Downloaded from https://www.cambridge.org/core. 19 Nov 2026 at 16:04:28, subject to the Cambridge Core terms of use.

Nevertheless, these studies are conducted on moderate ICDs with a slope $\Delta R/L \approx 0.5$. In contrast, DLR focused on the research on highly aggressive ICDs with a slope $\Delta R/L$ in the range of $0.75 - 1$, as shown in Dygutsch [8]. Therefore, DLR operates a unique ICD rig in Cologne, presented in Fig. 2a, to investigate the limits of further shortening. The rig is designed without any rotating components. A swirler row simulates an upstream LPC rotor by introducing swirl to the inflow. In the past, two ICDs with different axial lengths have been tested. Kasper [9–11] showed that both designs do not have any separations at the ICD hub. Thus, conventional ICDs can be designed more aggressively.



(a) ICD rig in cologne (Kasper [11]). (b) TU Berlin ICD rig (Fritz [1]).

Figure 2. *Comparison of the different ICD rigs.*

However, the shortening reaches a physical limit. At some point, separations become unavoidable. A promising concept to enable further shortening is the implementation of flow control methods in the ICD. For example, Naylor [3] and Stürzebecher [12] investigate the possibility of endwall contouring on the hub to reduce pressure-induced separations.

For further investigation on flow control strategies, a new ICD test case (presented in Fritz [1]) was designed. This design has a hub corner separation and another separation in the passage. Various flow control methods have been explored on this design. Kaliyaperumal [13, 14] numerically investigated several control methods on this test case, such as splitter vanes on the strut, steady blowing or boundary layer suction on this test case. Another approach is the implementation of pulsed jet actuators (PJAs). This kind of active flow control generates pulsed jets by a self-sustaining oscillation. The huge advantage of this method is the increased efficiency of the actuation. Furthermore, no moving parts are required to achieve the pulsation, which improves reliability.

However, PJAs have been mostly investigated experimentally, for example in Bauer [15]. Thus, there is limited experience with the numerical simulation of PJAs in a complex flow field such as the ICD. Consequently, a down-scale version of the DLR ICD rig was set up at the TU Berlin (Fig. 2b) to acquire validation data for numerical simulations in an early design stage. As shown in Fritz [16], the data obtained with the down-scaled twin of the DLR ICD mitigates the risk of numerical modeling uncertainties in a numerical optimisation. Additionally, the possibility of successful testing of the PJAs at the DLR test facilities increases. Therefore, the objective of the TU Berlin rig is the simple and rapid replacement of different PJA outlet configurations. To facilitate rapid replacement, the test rig is highly modular and mainly additively manufactured. The setup of the rig and the measurement results of the different configurations are shown in Bresemann [17]. Furthermore, the rig is more cost-efficient to operate because of the significantly lower mass flow rates.

Additionally, the ICD geometry developed by Fritz [1] was implemented in the full-scale ICD test rig at DLR. In an extensive test campaign, the flow field of the ICD was measured in detail for different Mach numbers and operating conditions. Therefore, the objective of the paper is to evaluate the design process of the DLR ICD; the study traces the design process backward and identifies differences in every step. Starting from a detailed analysis of the measurement data of the DLR ICD rig, the experimental

Downloaded from https://www.cambridge.org/core. 19 Nov 2026 at 16:04:28, subject to the Cambridge Core terms of use.

results are compared with numerical simulations. Furthermore, the experimental data of the small-scale rig are compared with those of the full-scale rig. This consideration helps to clarify how small-scale test rigs can support the design of future turbomachinery components by providing validation data in an early design stage.

2.0 Experimental setup

The ICD test rig of the DLR (Fig. 2b) is an annular cascade wind tunnel. It was specifically designed to investigate the effects of a length reduction of the ICD. The schematic setup of the test rig is presented in Fig. 3. A key feature of the test rig is the swirler row. This row introduces swirl and in this way simulates an upstream rotor. The swirler can also be adjusted to simulate the outflow conditions of the last LPC rotor. The test section contains three rows: LPC-outlet guide vanes (OGVs), a highly aggressive strutted ICD and HPC-inlet guide vanes (IGVs). The IGVs are also adjustable to simulate different upstream effects of an HPC. Another key feature is the bleed air extraction behind the OGVs. Therefore, the test rig is able to generate an engine-like inflow condition without any rotating components. The test rig has already been part of various publications, for example in Kasper [9–11], Fritz [16] and Wallin [18].

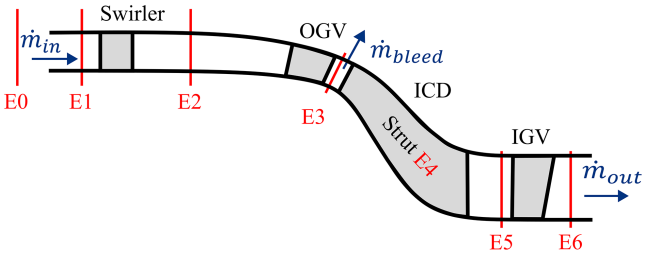


Figure 3. *DLR ICD rig setup and measurement planes (red lines) according to Kasper [10].*

2.1 Measurement techniques

The test rig features extensive measurement instrumentation in several measurement planes. The location of the measurement planes is shown in Fig. 3. The reference stagnation pressure $p_{t,\mathrm{E0}}$ and the reference stagnation temperature $T_{t,\mathrm{E0}}$ are measured in plane E0. The inlet conditions for the numerical simulations are determined in plane E1 with three pressure rakes and three temperature rakes. The dense distribution of the probes near the wall allows the pressure rake in Fig. 4 to measure the incoming boundary layer.

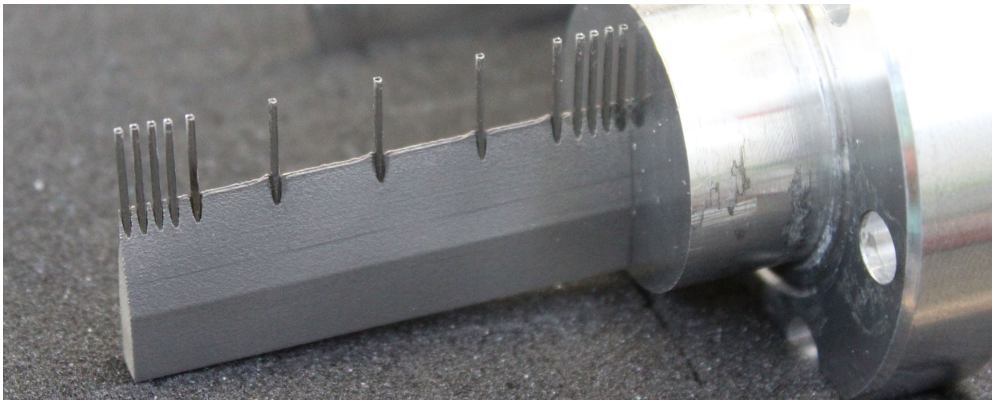


Figure 4. *Boundary layer rake of plane E1 and E2 (Kasper [11]).*

Downloaded from https://www.cambridge.org/core. 19 Nov 2026 at 16:04:28, subject to the Cambridge Core terms of use.

There is an additional boundary layer rake, similar to the one presented in Fig. 4, in plane E2. The rake can be rotated in the circumferential direction. Thus, the outflow pressure field of the swirler and consequently the inflow conditions of the OGVs can be determined.

The main evaluation plane is the ICD outflow plane, labeled with E5. This plane can also be traversed in the circumferential direction and is equipped with another boundary layer rake and a multi-hole probe (MHP). The two probes are positioned 1.5 passages apart to avoid interactions. The MHP is a dual-headed five-hole probe that can be traversed radially in addition to the circumferential direction. The two heads allow fast and efficient measurement of the ICD outflow.

2.2 MHP measurement mesh

The measurement mesh of the MHP is shown in Fig. 5. The mesh of the upper probe is plotted in grey, whereas the mesh of the lower probe is black. The green area represents an ICD passage, and the red line is the position of the upstream strut trailing edge. The upper and lower lines of the mesh are positioned a certain distance away from the walls. This safety distance is important to avoid collisions with the walls and interaction of the probe and the shaft with the boundary layer.

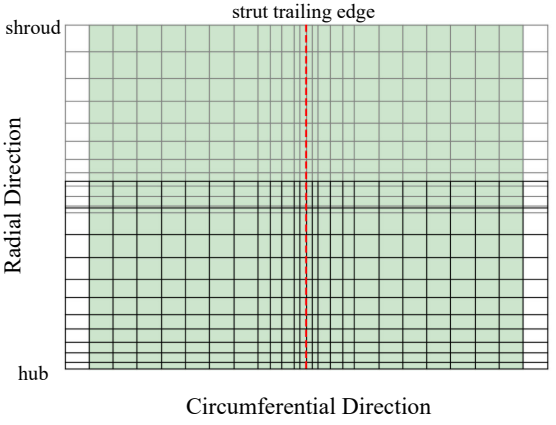


Figure 5. *Measurement mesh of the MHP traverse.*

Previous measurements at the TU Berlin rig in Bresemann [17] identified a thin wake that was difficult to capture. Thus, the measurement mesh was refined up to a resolution of 0.5 °behind the strut trailing edge to capture the wake in the DLR measurement campaign. Furthermore, the main task of the campaign was the detailed measurement of the hub region to provide a solid basis for the evaluation of flow control methods at the hub. Therefore, the mesh is also refined in the radial direction towards the hub. The mesh resolution has been validated with numerical data.

2.3 Measurement uncertainties

The measurement uncertainties of stagnation pressures were evaluated according to the Guide to the Expression of Uncertainty in Measurement (GUM) [19]. The measurement chain of the stagnation pressure comprises the ambient and the differential pressure measurement. In addition, the uncertainty of the MHP stagnation pressure $p_{t,\mathrm{E5,MHP}}$ also includes the model uncertainty associated with the multiparameter approximation. The combined uncertainty of the measurement chain was obtained using Gaussian error propagation. The uncertainty associated with the normalisation to the reference pressure $p_{t,\mathrm{E0}}$ was also included in the uncertainty propagation. The different uncertainties of the rakes originate from the

Downloaded from https://www.cambridge.org/core. 19 Nov 2026 at 16:04:28, subject to the Cambridge Core terms of use.

use of different differential pressure transducers. Plane E1 uses a PSI5 module, whereas the other two planes use a PSI15 module. Furthermore, the MHP pressure measurement is performed using a PSI5 module, which results in lower uncertainty compared to that of the E5 rake. The uncertainties, listed in Table 2, correspond to the expanded uncertainty U, calculated with a coverage factor of ($k = 2$), representing an approximate confidence level of 95%. According to the MHP calibration, the uncertainty of the circumferential angle α measurement is $\pm 0.5^{\circ}$.

Table 1. *Measurement uncertainties for the different measurement techniques*

Measurement technique	Measurand	U
E1 rake	$p_{t,norm}$	± 0.00044
E2 rake	$p_{t,norm}$	± 0.00058
E5 rake	$p_{t,norm}$	± 0.00058
E5 MHP	$p_{t,norm}$	± 0.00048
E5 MHP	α	$\pm 0.5^{\circ}$

2.4 Operating point

The investigated operating point is similar to the aerodynamic design point (ADP) presented in Kasper [11] and Dygutsch [20]. The ADP has an inlet Mach number of 0.32 and a Reynolds number 3.6 Mio. The Reynolds number refers to the outer radius of the inlet plane E1. Three percent of the inlet mass flow was extracted as bleed air behind the OGVs. In the following, the measurement point of the ADP is called VRN104.

3.0 Experimental results at ADP

The highly instrumented DLR test rig enables the influence of the upstream and downstream rows on the ICD flow to be investigated. In this section, the measurement data of the ADP are evaluated in detail. Therefore, this section is divided into two parts. In the first part, the inflow conditions are considered. Secondly, the outflow of the ICD is analysed to obtain insights into the flow structures in the ICD.

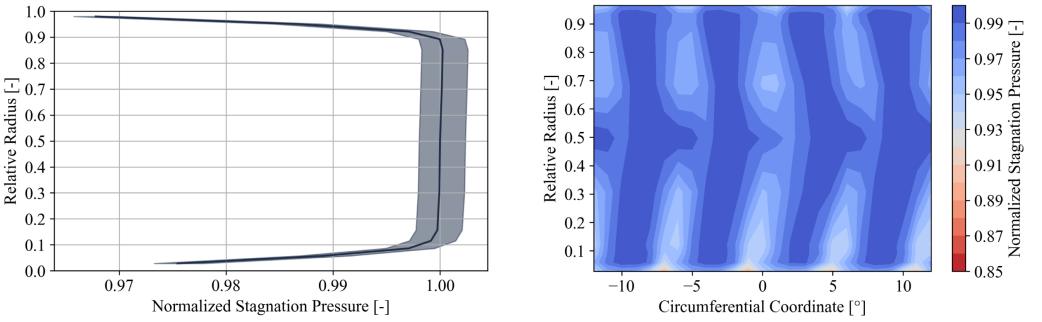
3.1 Inflow conditions

The inflow conditions of the swirler are measured in plane E1. The time-averaged stagnation pressure profile, determined with the boundary layer rake in Fig. 4, is shown in Fig. 6a. The profile has the typical shape of an undisturbed annular flow with a developed boundary layer at the walls. Outside of the wall regions, the stagnation pressure is almost constant over the radius.

The coloured band highlights the area between the minimum and maximum measured pressure during the testing time of the measurement point VRN104. The width of the band is a measure of the stability of the operating point. This consideration is important to ensure that the inflow conditions are stable during longer measurement times. Long measurement times occur if a planar traversing of the MHP is conducted, as done for the ADP presented in Fig. 6a. The measurement time for this operating point was approximately 90 minutes. The small deviations of less than 0.2% show that the inlet conditions were highly stable during this long measurement time.

Figure 6a shows the flow field in plane E2 behind the swirler. The plot contains four swirler passages with the corresponding wakes. As already shown by Fritz [16], the swirler introduces a strong secondary flow field. The flow through the partial gap intensifies the horseshoe vortices and leads to very defined round loss regions. Therefore, the OGVs experience a non-uniform inflow. The numerical studies of Fritz [16] concluded that the interaction of the secondary flow system of the swirler with the OGVs causes separations on the OGVs. The resulting losses are convected towards the hub by the radial

Downloaded from https://www.cambridge.org/core. 19 Nov 2026 at 16:04:28, subject to the Cambridge Core terms of use.



(a) Boundary layer rake in E1 (b) Boundary layer rake in E2

Figure 6. *The inflow conditions of the ICD are measured in plane E1 and E2 with boundary layer rakes.*

pressure gradient in the first bend. This effect destabilises the hub boundary layer and could cause an earlier onset of the separations.

3.2 Outflow conditions

The measurement plane E5 is instrumented with an MHP and a boundary layer rake to determine the ICD outflow conditions. The measurement data from this plane can be used to draw conclusions about the flow conditions and, in particular, the separations in the ICD. Figure 7 presents the normalised stagnation pressure field measured with the MHP. In the radial direction, the MHP cannot measure the regions close to the wall because of a required safety distance.

The pressure field in Fig. 7 shows the typical structure of a highly aggressive ICD. The flow field is asymmetric, and the wake is bended. There is also a loss region on the right side of the wake ① close to the hub. This loss region is typically caused by a corner separation at the right hub corner. Another distinct loss region ② is located on the left side of the wake between $-30\,^{\circ}$ and $-25\,^{\circ}$. These losses are generated by a separation in the ICD passage close to the left side of the strut.

The shroud region has a very high loss level throughout the circumference, except the region from -30° to -25° ③. In this region, a strong vortex should exist. This vortex represents the left leg of the upper strut horseshoe vortex. But this region is too disturbed for the MHP. The flow is misaligned, and the probe cannot capture the strong horseshoe vortex in this area.

The boundary layer rake in plane E5 is also traversable in the circumferential direction. Thus, a stagnation pressure field similar to the one measured with the MHP in Fig. 7 can be derived from the

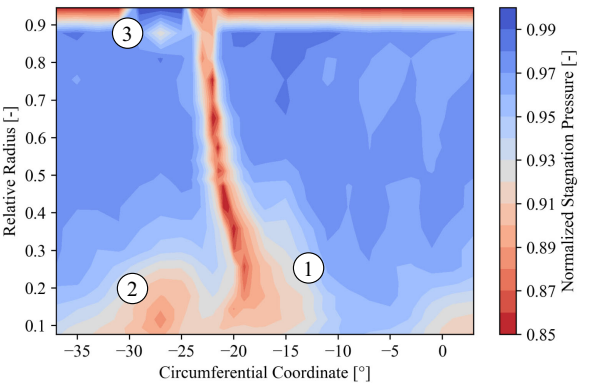


Figure 7. *Normalised stagnation pressure field at the ICD outlet measured with the MHP.*

Downloaded from https://www.cambridge.org/core. 19 Nov 2026 at 16:04:28, subject to the Cambridge Core terms of use.

rake data. The normalised stagnation pressure field of the boundary layer rake is shown in Fig. 8. The flow structure is identical to the field measured with the MHP in Fig. 7. The wake is less resolved in the circumferential direction because of the difference between both measurement devices of 1.5 passages. Therefore, the wake is now located in coarse areas of the measurement mesh (compare Fig. 5). Furthermore, the boundary layer rake has a coarser resolution of the mean flow.

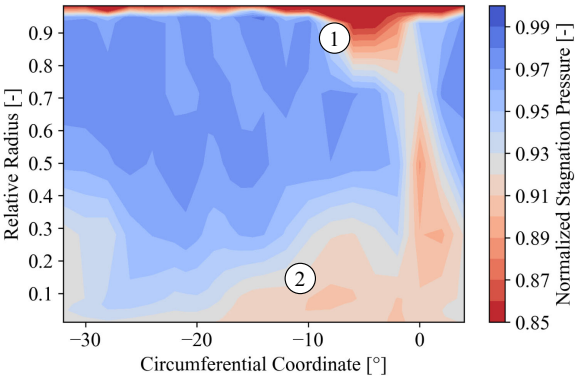


Figure 8. *Normalised stagnation pressure field at the ICD outlet measured with the boundary layer rake.*

However, further information about the flow conditions close to the walls is provided by the rake. At the shroud, the left leg of the horseshoe vortex ① is clearly visible. This loss region cannot be captured by the MHP because the secondary flow is so strong that the probe is misaligned with the flow. Furthermore, the loss region ② at the hub on the left side of the wake has a significantly larger circumferential expansion than measured with the MHP. The loss region ranges from $-18\,^\circ$ until the wake and covers almost half a passage. The MHP cannot measure in this region because of the safety distance to the wall. The presence of this loss region is a clear indication of a separation in the right part of the passage (aft-lookingforward (ALF)).

Finally, the pressure fields of the rake and the MHP are area-averaged over the circumference. Figure 9 compares the resulting stagnation pressure profiles. The shaded uncertainty band represents the expanded uncertainty with a coverage factor of $k = 2$ according to Table 1. The profiles are in very good agreement, especially in the lower half of the channel. The MHP profile is more detailed because of the larger number of radial measurement positions. Especially in the region of 10–20% channel height, the profile provides more information about the shape of the stagnation pressure distribution. On the other side, the rake data are a perfect extension of the MHP profile below 10% channel height. With increasing radius, the differences increase. A cause is the averaging method. The averaging is conducted with cell-averaged values. Thus, the average pressure is an average of values from two different radial heights. This could lead to differences in regions of large gradients and coarse resolution. The pressure profiles are further influenced by the different resolution of the wake. The comparison highlights the advantages of both measurement techniques. The rake provides detailed information about the regions close to the walls where the MHP cannot operate. However, the radial resolution of the MHP can be easily adapted to resolve regions of interest. Therefore, both methods are highly complementary.

The huge advantage of the MHP measurement is the calculation of the flow angles. The planar distribution of the circumferential flow angle α is shown in Fig. 10. The wake of the strut is again clearly visible ① as a shear layer. On the left side of the wake, the flow angle is positive, on the right side negative. At the hub, there is a huge gradient between positive and negative flow angles ② at around $-27\,^\circ$. This location coincides with the high-loss region left from the wake in Fig. 7. The sharp gradient between negative and positive angles is an indication of a strong streamwise vortex. The vortex core aligns with the centre of the losses ② in Fig. 7.

Downloaded from https://www.cambridge.org/core. 19 Nov 2026 at 16:04:28, subject to the Cambridge Core terms of use.

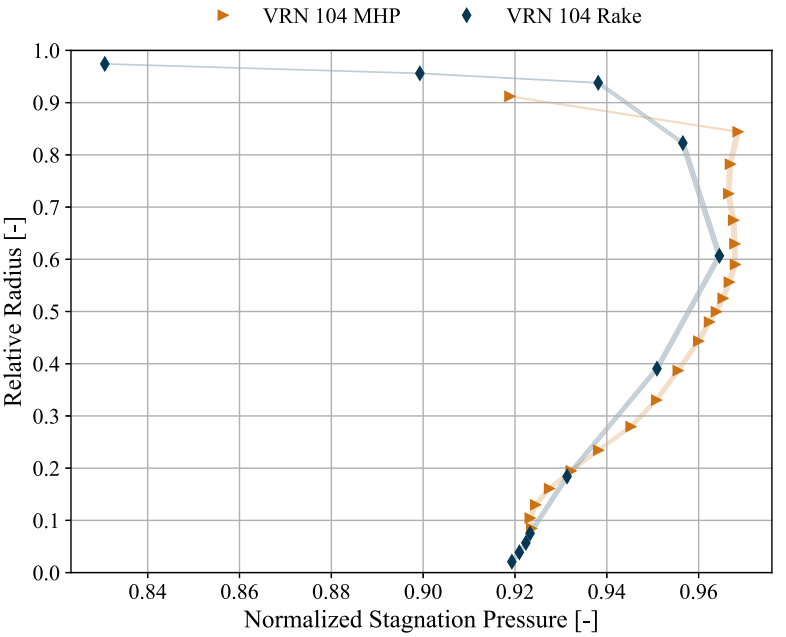


Figure 9. *Comparison of the normalised stagnation pressure profiles in plane E5 measured with the boundary layer rake and the MHP.*

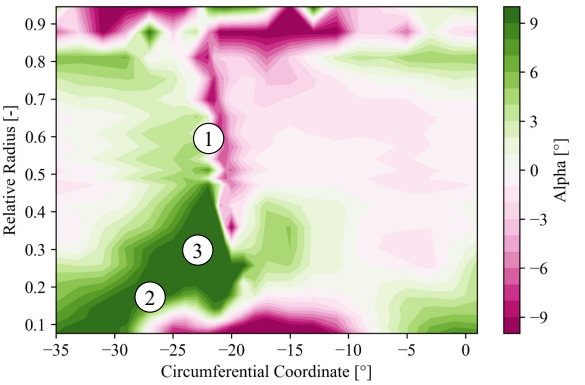


Figure 10. *Circumferential angle α field in plane E5. An angle $\alpha = 0$ is equivalent to a purely axial flow.*

A large region of high negative flow angles occurs at the shroud and the hub. Also, there is a region of high positive flow angles ③ on the left side of the wake. Thus, the flow field shows on a constant radius large deviations and gradients of the circumferential flow angle α. The highly inhomogeneous flow field could influence the performance of the downstream HPC.

4.0 Numerical simulation of the ADP

The flow solver used for the numerical simulations is TRACE [21]. TRACE is developed and validated at the DLR Institute of Propulsion Technologies in the Department for Numerical Methods [22, 23] in close collaboration with MTU Aero Engines. The simulations use the density-based finite-volume

Downloaded from https://www.cambridge.org/core. 19 Nov 2026 at 16:04:28, subject to the Cambridge Core terms of use.

branch of this solver. The steady Reynolds-averaged Navier Stokes (RANS) simulations are conducted with three different turbulence models:

- shear-stress transport (SST) model [24]
- Hellsten explicit algebraic Reynolds stress modeling (EARSM) [25]
- SSG-LRR Reynolds-stress model (RSM) [26]

The numerical setup is similar to the one presented in Fritz [1] and represents one ICD passage with the corresponding blade numbers of the adjacent rows. Thus, the setup includes 6 swirler vanes, 12 LPC-OGVs and 3 HPC-IGVs. The four rows are connected by zonal interfaces. This type of interface exchanges fluxes by interpolation and allows the connection of rows with different meshes. Therefore, every row in the numerical setup must cover the same angle range. The resulting multi-passage setup is important to capture the interactions between the components. The domain was meshed as a structured multiblock mesh with AUTOGRID. The mesh is constructed as a low-Reynolds mesh with a dimensionless wall coordinate y^+ of about 1 and contains about 32 Mio. cells.

4.1 Boundary conditions

The inlet conditions for stagnation pressure and stagnation temperature are derived from the measurements. Pressure and temperature rakes are installed in inlet plane E1. Kasper [10] has already shown that the inflow conditions are uniform. Therefore, the data are time-averaged and prescribed as radial profiles. Figure 6a shows the stagnation pressure profile used as a boundary condition. Furthermore, a purely axial inflow is assumed. The turbulence intensity and turbulence length scale were taken from previous hot-wire measurements for the same operating point, conducted by Kasper [10].

Mass flow measurements are applied in the ICD rig for inlet and bleed mass flow rate via orifice flow meter sections. The difference between both measurement is time-averaged and prescribed as an outlet boundary condition. Furthermore, a bleed mass flow rate of 3% is extracted behind the OGVs.

4.2 ICD outlet pressure distribution

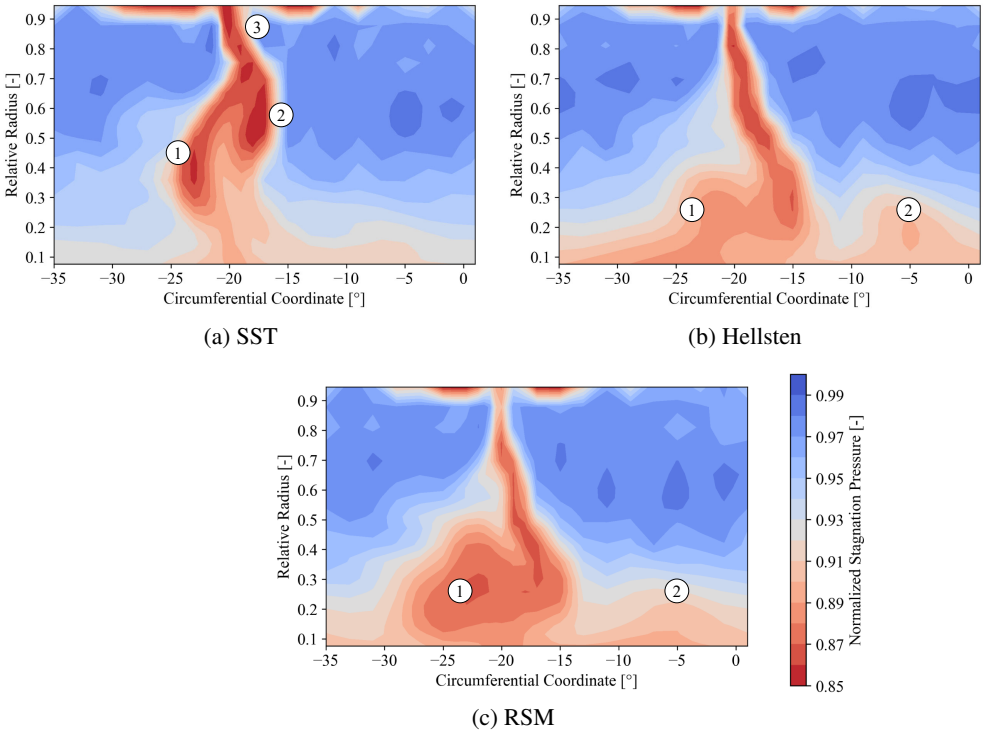
The results of the numerical simulation with different turbulence models are presented in Fig. 11. The plots show the normalised stagnation pressure field in plane E5. The results are interpolated on the experimental mesh to achieve comparability with the experimental fields in Figs 7 and 8. Thus, the regions close to the walls are also excluded. The position of the wake in the numerical plots is identical to the position in the MHP measurements in Fig. 7.

The structure of the SST pressure field in Fig. 11a shows significant deviations from the experimental data (Fig. 7). The shape of the wake is fundamentally different. The wake is wider, and loss regions of elliptical shape occur at around 40% channel height on the left side ① and at around 50–60% on the right ② of the strut. These losses are caused by the horseshoe vortex on the hub of the strut. Thus, the lower horseshoe vortex separates from the hub on both sides. This behaviour is not observed in the experiments. Furthermore, the upper part of the wake ③ differs from the experiments and the other simulations. The loss level is higher, and the wake is wider above 80% channel height.

The pressure field of Hellsten (Fig. 11b) and RSM (Fig. 11c) are similar. Both simulations show a flow structure that is similar to the experiments. For both simulations, the wake is bent, and a round loss region occurs on the left side of the wake ①. The loss region is predicted closer to the strut trailing edge than measured in the experiments. The centre of this loss region is located between -25° and -20° in both simulations and not between -30° and -25° observed in the experimental data. Thus, the numerical simulations show a discrepancy of about 5° in the circumferential position of this loss region. Furthermore, the loss region is larger and has higher losses for the RSM simulation (Fig. 11c). Among all turbulence models, the Hellsten model agrees best with the experimental data in Fig. 7.

Downloaded from https://www.cambridge.org/core. 19 Nov 2026 at 16:04:28, subject to the Cambridge Core terms of use.

However, the loss region around -5° ② cannot be observed in the experimental data in Fig. 7. The loss region occurs in both the RSM and Hellsten simulations. The region is more defined in the Hellsten simulation. In contrast, this region has a very low loss level in the experiments. Thus, the numerical simulation predicts another loss mechanism that cannot be observed in the experimental data.



(a) SST (b) Hellsten

(c) RSM

Figure 11. *Comparison of the stagnation pressure field in plane E5, calculated with different turbulence models.*

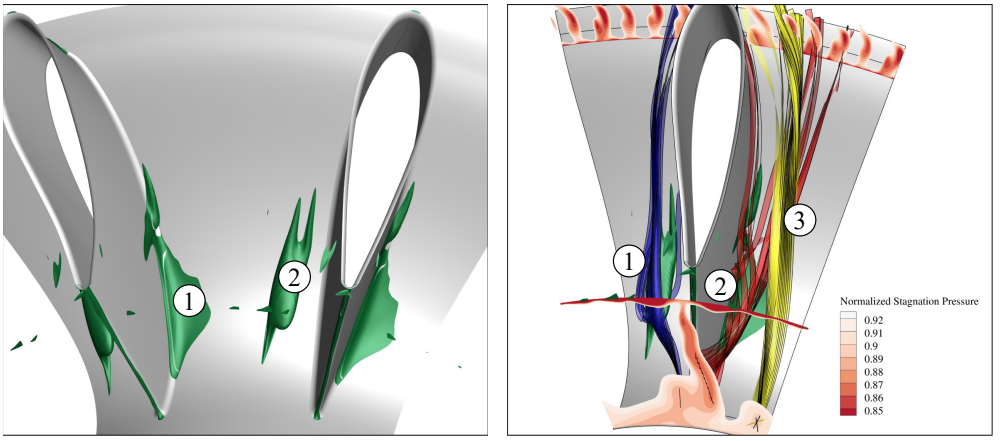
4.3 Separation topology

The numerical simulations have the huge advantage that a three-dimensional volume can be investigated. Every point in the numerical domain is accessible. Besides the uncertainties in the turbulence modeling, the simulations are a valuable tool for visualising flow structures. The experiment at the DLR rig cannot visualise the topology of the separations in the ICD. Only the effects of the separations can be observed in the stagnation pressure field at the outlet plane E5 as regions of high loss levels.

Figure 12 shows two different analyses of the flow field in the Hellsten simulation. The view is against the flow direction (ALF). The simulation using the Hellsten turbulence model was selected, as the previous section showed that it provides the best agreement with the experimental data. Figure 12a visualises the separations in the ICD by iso-surface with the criterion $v_x < 0$. The hub boundary layer experiences two distinct separations. A hub corner separation ① occurs at the right side of the strut (ALF). Another separation bubble ② forms in the passage close to the left side of the strut.

The numerical simulations enable the losses to be linked to distinct flow mechanisms. Thus, Fig. 12b investigates the origin of the loss regions in plane E5. The normalised planar stagnation pressure distribution in plane E5 is shown in the figure. The regions with $p_{t,norm} > 0.92$ are transparent to provide a better view of the flow field. Also, the incoming losses are visualised in the same manner. The streamlines illustrate the origin of the losses. Blue streamlines ① are linked to the loss region on the left side of the wake. The losses are associated with the passage separation. The origin of the losses on the right

Downloaded from https://www.cambridge.org/core. 19 Nov 2026 at 16:04:28, subject to the Cambridge Core terms of use.



(a) Separation topology (b) Origin of the loss regions

Figure 12. *Flow field of the simulation with the Hellsten turbulence model (ALF). Green surfaces visualise negative axial velocities $v_x < 0$ and thus, flow separations. The streamlines indicate the origin of the losses in Fig. 11.*

side of the wake is highlighted with red streamlines ②. These losses are generated by the hub corner separation.

The previous paragraph concludes that the numerical simulations (Hellsten and RSM) contain another loss mechanism that is responsible for the loss region at $-5\,^\circ$ in Fig. 11b and c. Yellow streamlines ③ visualise the origin of these losses. The losses are not associated with any separation in the ICD but rather with a specific OGV wake. The loss mechanisms of the upstream components have already been described in Section 3.1 and Fritz [16]. The interaction of the swirler secondary flow system with the OGVs causes larger flow separations on every second vane. Furthermore, the upstream effect of the strut enhances the separations on the OGVs ahead of it. These effects generate the incoming loss region that later forms the loss region ② in Fig. 11b and c. In summary, the numerical simulations struggle to predict either the loss generation upstream of the strut or the development of the incoming losses in the ICD.

4.4 Radial stagnation pressure profile

The analysis of the numerical stagnation pressure field in Fig. 11 identified differences in the flow structure. However, a quantitative comparison requires the evaluation of the radial profiles. Therefore, the numerical results were circumferentially area-averaged. The comparison of the resulting stagnation pressure profiles is shown in Fig. 13. All numerical methods overestimate the losses in the ICD. Especially the SST turbulence model predicts higher losses between 70% and 85% channel height. This region is not significantly affected by secondary flow phenomena. The reason for the higher losses is the wider wake in Fig. 11a. The Hellsten and RSM turbulence models are able to reproduce this region in very good agreement with the experimental data. Notably, the predicted losses in the end wall regions for the SST model show good agreement with the experimental data.

The pressure profiles of Hellsten and RSM show the same characteristics. Above 70% channel height, the profiles are very close to the experimental data. The shape of the Hellsten profile is similar to the experimental data below 70% channel height. However, the simulations overpredict the losses in the lower part of the channel. The same behaviour is observed in Fig. 11b and c, where the loss level in the lower part of the wake is higher than in the experiments in Fig. 7. Nevertheless, the shape of the Hellsten

Downloaded from https://www.cambridge.org/core. 19 Nov 2026 at 16:04:28, subject to the Cambridge Core terms of use.

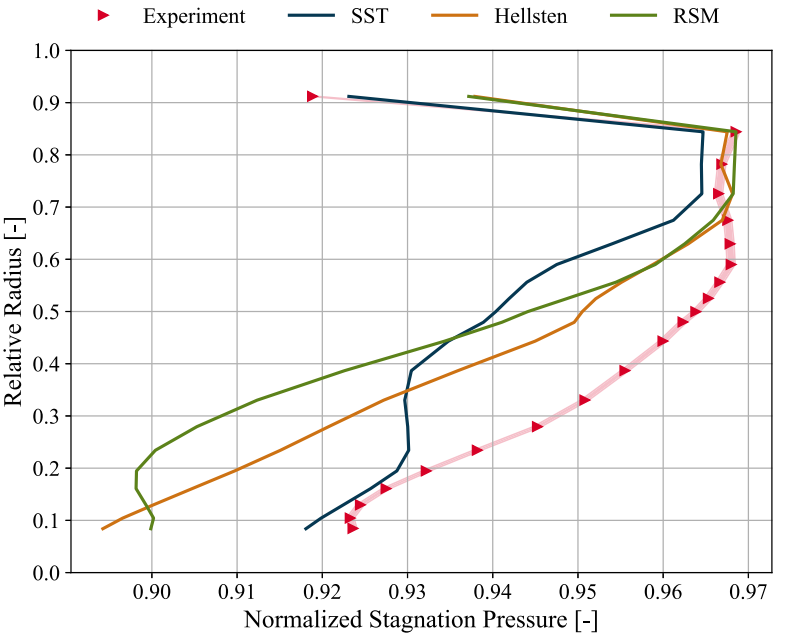


Figure 13. *Comparison of the numerical and experimental radial stagnation pressure profiles in plane E5.*

pressure profile is similar to the experimental data. This again highlights that the simulations struggle to accurately reproduce the losses in the ICD.

4.5 ICD pressure losses

Finally, the stagnation pressure loss ω is calculated according to Equation (1) via area-averaging the normalised stagnation pressure field for the experiment and the simulations.

$$\omega = 1 - \frac{p_{t,\mathrm{E5}}}{p_{t,\mathrm{E0}}} \tag{1}$$

Table 2 lists the stagnation pressure losses for the different turbulence models and their difference to the measured value in percent. The stagnation pressure loss measured with the MHP is 0.031. The stagnation pressure losses in Table 2 underline the finding of the previous section. The numerical simulation is significantly overestimating the losses in the ICD. The RSM turbulence model predicts losses that are almost twice as high as the measured value. Although the other turbulence models yield lower losses, the deviation from the measured value remains very high at over 80%.

Table 2. *Comparison of the numerical stagnation pressure losses with the measured loss*

Turbulence model	ω	$\Delta\omega$ (%)
SST	0.058	87
RSM	0.061	97
Hellsten	0.057	84

5.0 Comparison of the twins

The ICD rig of the TU Berlin is a simplified and down-scaled twin of the DLR ICD rig with a scaling factor of 2.55. Figure 14 shows the setup and the measurement planes of the TU Berlin rig. The rig does

Downloaded from https://www.cambridge.org/core. 19 Nov 2026 at 16:04:28, subject to the Cambridge Core terms of use.

not include a swirler and an IGV row. The OGV row was modified to achieve a similar flow field of the ICD without an upstream swirler row. The row also has half the number of vanes because of manufacturing reasons. Also, the rig is not equipped with a bleed system. However, both test rigs can operate at the same inlet Mach number. The Reynolds number is approximately 1.8 million and is therefore only half as high as for the DLR rig. However, previous investigations of Fritz [1] concluded that the Reynolds number is sufficiently high that its influence can be neglected. Consequently, the operating points of both rigs are assumed to be comparable. Furthermore, the axial positions of the measurement planes are equal to the down-scaled positions of the DLR rig in Fig. 3. In plane E5, an MHP measurement is also conducted with a mini five-hole probe and a circumferential and radial traversing system. This section will therefore examine the difference of these two test rigs.

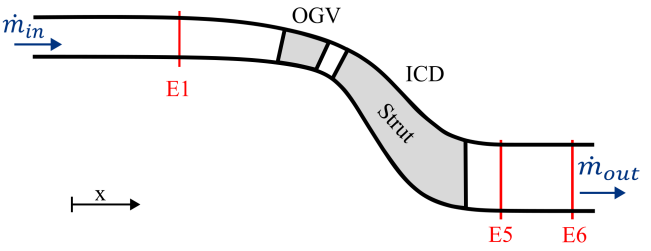


Figure 14. *TU Berlin rig setup and measurement planes (red lines).*

5.1 Outlet flow field

Figure 15 shows the Mach number field in the ICD outlet plane E5 of the TU Berlin ICD, measured with an MHP. The Mach number field is used to demonstrate that both rigs operate at comparable Mach number levels and to illustrate the distribution of dynamic pressure within the flow field. The trailing edge of the ICD is at the 0° position (dashed line). Of particular note are the extensive regions of low Mach numbers observed at the shroud ①③. These regions are related to a very strong horseshoe vortex. Furthermore, this counter-rotating vortex pair generates a large separation accompanied by high losses at the shroud, as shown in Bresemann [17] and Fritz [27]. Another region of low Mach number ② is observed on the right side of the trailing edge in the lower part of the channel. This region results from a strong hub-corner separation. An additional small region of low Mach numbers ④ appears at the hub at around −10°. The cause of this region is a small passage separation.

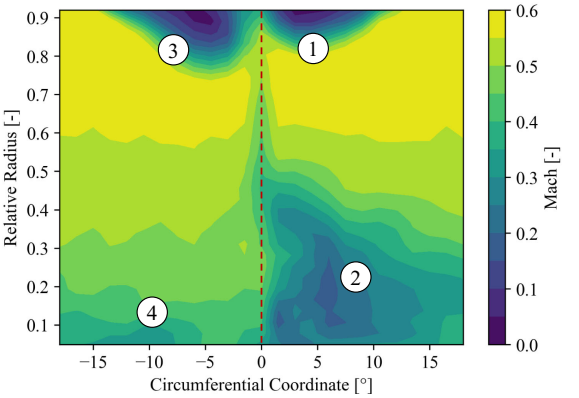


Figure 15. *Outlet Mach field of the scaled TU Berlin ICD.*

Downloaded from https://www.cambridge.org/core. 19 Nov 2026 at 16:04:28, subject to the Cambridge Core terms of use.

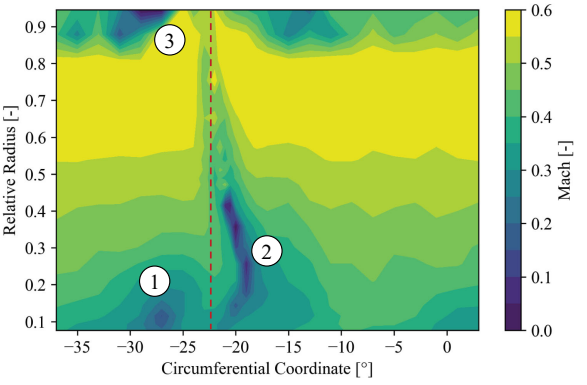


Figure 16. *Outlet Mach field of the full-size DLR ICD in plane E5.*

The Mach number field of the DLR ICD rig is shown in Fig. 16. The trailing edge of the ICD is at around −22° (dashed line). A low Mach number region ① appears at the hub between −30° and −25°. This region originates from the passage separation. Also, the right hub corner has a region of reduced Mach number ②. The hub-corner separation causes this loss region. However, the region is reduced compared to the TU Berlin rig. In summary, the passage separation is stronger for the DLR ICD rig while the hub-corner separation is smaller.

In both rigs, the left side of the upper horseshoe ③ is pronounced. Furthermore, the horseshoe vortex is significantly weaker in the DLR ICD rig, and the shroud separation is considerably smaller. This finding supports the assumption of Fritz [27] that the presence of an HPC-IGV row would significantly reduce the size of the shroud separation of the TU Berlin rig. Thus, the shroud separation of the TU Berlin is not representative for a highly aggressive ICD in a jet engine environment.

5.2 Radial stagnation pressure profile

Finally, both rigs can be compared by the stagnation pressure profiles at the ICD outlet. Figure 17 shows the measured radial stagnation pressure distribution. The uncertainty of the TU Berlin pressure measurement is 0.05%. Furthermore, the combined uncertainty of the normalisation is obtained using Gaussian error propagation. The shaded uncertainty band again represents the expanded uncertainty for both rigs. The setup of the TU Berlin does not include a swirler row. In order to ensure a fair comparison between both rigs, the stagnation pressure of the DLR ICD is normalised by the average stagnation pressure of plane E2 $p_{t,\mathrm{E2,0D}}$. Thus, the control volume includes the OGVs and the ICD.

The effect of the shroud horseshoe vortex in the TU Berlin rig is also reflected in the stagnation pressure profile. The losses are significantly higher in this region. The radial extent of the shroud loss region is also larger. In the TU Berlin rig, the loss region extends down to 60% channel height, whereas in the DLR rig, the region only reaches down to 85%. Beneath the shroud loss region, there is a maximum in the stagnation pressure profile. For the DLR rig, this maximum is a region of almost constant pressure from 60% to 85% channel height. The maximum for the TU Berlin rig is round with a peak around 60%. Below 50% channel height, the shape of the profiles is similar. The losses increase monotonically towards the hub until 10%. Especially, the local minimum at this height exists in both profiles. Thus, the loss generation of the TU Berlin below 50% channel height is representative of the full-scale DLR ICD rig. Consequently, the TU Berlin is suitable for the investigation of flow control methods on the ICD hub. The transferability of the results to the DLR rig is ensured by the similarity of the flow structures.

It is noteworthy that the losses of the DLR ICD are higher than those of the TU Berlin ICD except in the shroud region. Especially below 50% channel height, the pressure profiles seem to be shifted by a constant value. The reason for this is the OGV row. The OGVs of the DLR rig are highly loaded due to the

Downloaded from https://www.cambridge.org/core. 19 Nov 2026 at 16:04:28, subject to the Cambridge Core terms of use.

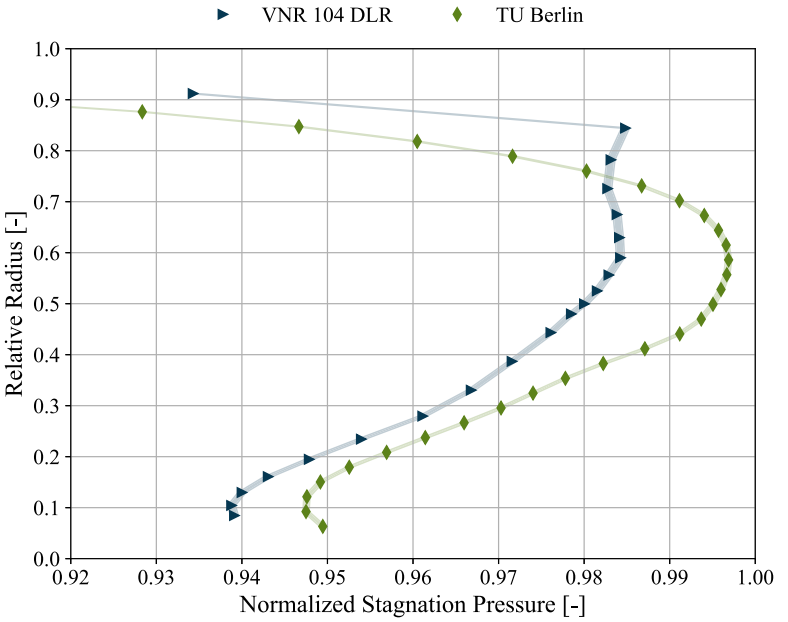


Figure 17. *Comparison of the radial outlet stagnation pressure distribution of the twins.*

preswirl introduced by the swirler. The TU Berlin rig operates without preswirl and, thus, the OGVs are significantly less loaded. Furthermore, the DLR ICD features double the number of OGVs. The larger wetted surface increases the friction losses in this row. In addition, the secondary flow system of the swirler induces alternating separation on the OGV suction side. This effect has already been investigated in Fritz [16] for the DLR ICD rig and visualised in Fig. 12b. These separations cause further losses. CFD simulations conducted with the Hellsten turbulence model conclude that the losses of the DLR OGV are more than 15 times higher than the TU Berlin OGV losses. Thus, the differences in the OGV row mainly cause the higher loss level of the DLR ICD outside the shroud region.

6.0 Conclusion

A detailed analysis of the measurement data was carried out, accompanied by a comparison against numerical simulations and measurements from the down-scaled twin test rig at TU Berlin. The following conclusions can be drawn from the study:

1. The stagnation pressure fields of the ICD, measured with the MHP and boundary layer rake, show clear indications of flow separations in the ICD. The comparison of the radial distribution of the MHP and the boundary layer rake in Fig. 9 showed good agreement. Furthermore, the boundary layer can be resolved, which provides additional information about the horseshoe vortex at the shroud. Due to the circumferential position of the boundary layer rake, the wake area is not well resolved. Thus, future test campaigns could introduce a measurement point specifically for a boundary layer traverse. The circumferential spacing could be optimised to capture the wake region of the strut. This measure could reduce the measurement time from 90 to 5 minutes for operating points where a detailed investigation with the MHP is not required.
2. Additionally, the MHP measured a strongly disturbed circumferential angle α at the ICD outlet. This disturbance could influence the downstream HPC. Thus, the implementation of flow control methods should consider a reduction in the outflow disturbance as another objective.

Downloaded from https://www.cambridge.org/core. 19 Nov 2026 at 16:04:28, subject to the Cambridge Core terms of use.

Furthermore, future test campaigns could use high-speed optical measurement techniques to capture the high unsteadiness in the ICD outflow.

3. The comparison of the experimental and numerical data in Section 4 showed an overprediction of the losses generated by the separations in the numerical simulations. Furthermore, the losses generated by the interaction of the strut with the upstream components form another loss region that cannot be observed in the experiment. Thus, the measured losses are lower than expected in the numerical design of the ICD. Consequently, relying only on numerical data could lead to a very conservative design. The potential for further shortening could not be achieved due to the overprediction of losses.
4. All considered turbulence models struggle to predict the flow structures in the ICD in a good agreement with the measurement data. Only the Hellsten turbulence model is close to the measurement data, but it still predicts a loss region, which could not be observed in the experiments. Nevertheless, the losses in the ICD are overpredicted by more than 80%. This may indicate that unsteady flow phenomena play a stabilising role, potentially contributing to reduced loss levels. Consequently, the flow field of a highly aggressive ICD is difficult to predict accurately using steady RANS simulations, which do not account for unsteady flow phenomena. Future research should consider whether hybrid simulation approaches such as Delayed Detached Eddy Simulation (DDES) or scale-resolving simulations such as LES can provide a reliable prediction of the separations in the ICD. A reliable prediction of the separation onset in an ICD could expand the design space towards more aggressive designs.
5. The comparison of the measurement data of both twins shows clear differences. These differences are mainly observed in the shroud region and the OGV losses. However, the TUB rig reproduces the characteristic flow structures in the lower part of the ICD. In particular, these flow structures are relevant for investigating flow control on the hub. Therefore, the TUB rig provides an appropriate simplified configuration for developing and assessing active flow control concepts on the ICD hub. The developed concepts can be transferred and adapted to the full-scale DLR test rig. In this way, the risk of the expensive full-scale experiment can be reduced. Future enhancement of the TUB rig could focus on improving the comparability. A swirler row could be designed to simulate the LPC rotor. This change would also require the design of new, higher-loaded OGVs. In addition, the design of HPC-IGVs could suppress the larger shroud separations in the TU Berlin rig.

In conclusion, the chosen design approach has proven to be successful. The numerical simulation of an aggressive ICD is very challenging and leads to an overestimation of the losses. Thus, experimental data are necessary to validate the numerical setup and the turbulence model. Therefore, small-scale rigs such as the TU Berlin ICD rig can mitigate the numerical uncertainties by providing experimental validation data in an early design stage.

Acknowledgements. The research reported in this paper was performed under the RDUCT project of the German Aviation Research Program (LuFo VI-2, grant number 20Q2110C) and is funded by the Federal Ministry for Economic Affairs and Climate Action. The authors gratefully acknowledge the scientific support and HPC resources provided by the German Aerospace Center (DLR). The HPC system CARO is partially funded by 'Ministry of Science and Culture of Lower Saxony' and 'Federal Ministry for Economic Affairs and Climate Action'.

References

[1] Fritz, S., Hergt, A., Bresemann, D., Eck, M. and Peitsch, D. On the performance of highly aggressive inter compressor ducts, *Aeronaut. J.*, 2025, **129**, (1335), pp 1125–1141.

[2] Ortiz Dueñas, C., Miller, R.J., Hodson, H.P. and Longley, J.P. Effect of length on compressor inter-stage duct performance, *Volume 6: Turbo Expo 2007, Parts A and B, ASMEDC*, 2007, pp 319–329.

[3] Naylor, E.M.J., Ortiz Dueñas, C., Miller, R.J. and Hodson, H.P. Optimisation of non-axisymmetric endwalls in compressor S-shaped ducts, *Volume 6: Turbomachinery, Parts A, B, and C, ASMEDC*, 2008, pp 305–316.

Downloaded from https://www.cambridge.org/core. 19 Nov 2026 at 16:04:28, subject to the Cambridge Core terms of use.

[4] Walker, A.D., Barker, A.G., Carrotte, J.F., Bolger, J.J. and Green, M.J. Integrated outlet guide vane design for an aggressive S-shaped compressor transition duct, *J. Turbomach.*, 2012, **135**, (1), p 011035.
[5] Walker, A.D., Barker, A.G., Mariah, I., Peacock, G.L., Carrotte, J.F. and Northall, R.M. An aggressive S-shaped compressor transition duct with swirling flow and aerodynamic lifting struts, *Proceedings of ASME Turbo Expo*, Volume 2A: Turbomachinery, 2014, p V02AT40A002.
[6] Wallin, F., Johansson, P. and Robertsson, T. Design of integrated turning vanes for a compressor transition duct, *ISABE* 2011, 2011.
[7] Mariah, I., Peacock, G.L., Carrotte, J.F., Walker, A.D. and Hall, C. Development of an integrated lifting strut and outlet guide vane in a compressor transition duct, *Proceedings of ASME Turbo Expo*, Vol. 11, 2025, p V011T33A006.
[8] Dygutsch, T., Kasper, A. and Voss, C. On the effect of inter compressor duct length on compressor performance, *Aeronaut. J.*, 2022, **126**, (1302), pp 1333–1350.
[9] Kasper, A., Hergt, A., Stürzebecher, T., Grund, S., Flamm, J. and Nicke, E. Flow structure within an aggressive S-shaped intermediate compressor duct, *J. Phys.: Conf. Ser.*, 2021, **1909**, (1), pp 1–9.
[10] Kasper, A., Dygutsch, T., Grund, S., Beversdorff, M., Hakansson, S., Nicke, E. and Lejon, M. Experimental investigation of an aggressive S-shaped intermediate compressor duct, *Proceedings of ASME Turbo Expo*, Rotterdam, NL, 2022.
[11] Kasper, A. Experimentelle Untersuchung von Sekundarströmungsphänomenen in stark verkürzten Verdichterübergangskanälen, Technical Report No. 2025-12. Technische Universität Berlin, 2025. https://elib.dlr.de/214399/
[12] Stürzebecher, T., Goinis, G., Voss, C., Sahota, H., Groth, P. and Hammer, S. Automated aerodynamic optimization of an aggressive S-shaped intermediate compressor duct, *Proceedings of ASME Turbo Expo*, Oslo, NO, 2018.
[13] Kaliyaperumal, A., Glodic, N., Gutierrez Salas, M., Bergh, J. and Fritz, S. Influence of circumferential splitter vane on aerodynamics of super aggressive intermediate compressor duct, ISABE, Toulouse, FR, 2024.
[14] Kaliyaperumal, A., Glodic, N., Gutierrez Salas, M., Fritz, S., Hergt, A. and Bergh, J. A numerical investigation of active flow control strategies for the suppression of aerodynamic flow separations in a very aggressive intermediate compressor duct, *Proceedings of ASME Turbo Expo*, London, GB, 2024.
[15] Bauer, M. Design and application of a fluidic actuator system for high lift flow control, Technical report no. Technische Universität Berlin, 2015.
[16] Fritz, S., Dygutsch, T., Kasper, A., Hergt, A., Grund, S., Flamm, J., Lejon, M. and Sahota, H. On the secondary flow system of an aggressive inter compressor duct, *J. Turbomach.*, 2024, **146,** (10), pp 1–11.
[17] Bresemann, D., Eck, M., Peitsch, D., Fritz, S., Hergt, A. and Rückert, R. Highly aggressive inter compressor duct with active flow control PART 1: Experimental validation of optimized pulsed jet actuators, *Proceedings of ASME Turbo Expo*, Memphis, TN, USA, 2025.
[18] Wallin, F., Langhoff, P. and Nicke, E. Aerodynamic test campaign of next generation aggressive intermediate compressor ducts, *ISABE*, Canberra, AU, 2019.
[19] JCGM. Evaluation of Measurement Data – Guide to the Expression of Uncertainty in Measurement. JCGM 100:2008, Joint Committee for Guides in Metrology, 2008.
[20] Dygutsch, T. Modulübergreifende aerodynamische Verdichterauslegung, Technical report no. DLR-FB-2024-3. Technische Universität Berlin, 2023. https://elib.dlr.de/202422/
[21] Department of Numerical Methods. TRACE Suite, 2023. https://doi.org/10.5281/zenodo.18184278
[22] Becker, K., Heitkamp, K. and Kügeler, E. Recent progress in a hybrid-grid CFD solver for turbomachinery flows, *Proceedings Fifth European Conference on Computational Fluid Dynamics ECCOMAS CFD*, Vol. 2010, 2010.
[23] Geiser, G., Wellner, J., Kügeler, E., Weber, A. and Moors, A. On the simulation and spectral analysis of unsteady turbulence and transition effects in a multistage low pressure turbine, *J. Turbomach.*, 2019, **141**, (5), p 051012.
[24] Menter, F.R., Kuntz, M. and Langtry, R. Ten years of industrial experience with the SST turbulence model, *Turbulence, Heat and Mass Transfer*, Vol. 4, 2003.
[25] Hellsten, A. New advanced k-w turbulence model for high-lift aerodynamics, *AIAA J.*, 2005, **43**, (9), pp 1857–1869.
[26] Cécora, R.-D., Radespiel, R., Eisfeld, B. and Probst, A. Differential Reynolds-stress modeling for aeronautics, *AIAA J.*, 2015, **53**, (3), pp 739–755.
[27] Fritz, S., Koppers, F., Hergt, A., Bresemann, D., Eck, M., Peitsch, D., Möller, F.M. and Rückert, R. Highly aggressive intercompressor duct with active flow control: Numerical validation of pulsed jet actuators with unsteady simulations, *J. Turbomach.*, 2025, **148**, (6), p 061004.

Cite this article: Fritz S. P., Hergt A., Grund S., Schlappa J., Bresemann D., Eck M. and Peitsch D. Experimental investigation of highly aggressive inter-compressor ducts. *The Aeronautical Journal*, https://doi.org/10.1017/aer.2026.10216

Downloaded from https://www.cambridge.org/core. 19 Nov 2026 at 16:04:28, subject to the Cambridge Core terms of use.